Nonlinear Coupling Coefficients in Multimode Fibers for the Strong Coupling Regime Within Mode Groups and Across Mode Groups

Paolo Carniello, Filipe M. Ferreira, *Senior Member, IEEE*, Norbert Hanik *Senior Member, IEEE*

***Abstract*—We study the nonlinear coupling coefficients appearing in the Manakov equations for multimode fibers (MMF) for space-division multiplexing operating in the two regimes of strong coupling only within mode groups and strong coupling also across mode groups. The analysis is mainly focused on the trenchless parabolic graded-index MMFs, but considerations on the step-index profile, and on the use of realistic trenches and non-parabolic indices are given. Analytic results for the Manakov nonlinearity coefficients are derived for the first time, and validation is performed through a numerical approach. We show that the coefficients are approximately independent on the fiber core radius and refractive index difference, but depend only on the number of guided modes. Values of nonlinear coefficients are computed also for optimized and manufactured MMFs described in the literature, and are placed within the developed framework. The impact of a poor fiber design on the achievable data rates of the MMF nonlinear channel is discussed for a simple scenario.**

***Index Terms*—Multimode fibers, space division multiplexing, Manakov equation, nonlinear coupling, optical communications.**

I. Introduction

In the field of space-division multiplexing (SDM) the most common fiber structures are multicore fibers (MCFs) and multimode fibers (MMFs). Based on the level of linear coupling among the fiber modes, two common operational regimes are distinguished: the intra-modal group coupling regime (IMGCR) and the strong coupling regime (SCR) [1]. In the IMGCR, modes belonging to the same modal group are assumed to be strongly-coupled, while modes of different groups are assumed to be uncoupled, as for MMFs with sufficient phase-mismatch among the modal groups as well as for weakly-coupled MCFs (WC-MCFs) [2]. In the SCR, all fiber modes are assumed to be strongly coupled, as for randomly-coupled MCFs (RC-MCFs)[3], and for graded-index multimode fiber (GIMMF) with suitable techniques to enhance coupling – e.g., using long period fiber gratings [4], [5], [6]. In long-haul communications it is often tried to achieve the SCR such that delay spread and mode dependent loss accumulate at a slower pace with transmission distance (e.g., ideally with the square-root of distance), compared to the case of partial coupling [7], [8], [9]. The level of coupling can be directly controlled in MCFs through, e.g., the separation of the cores [10], [11], while it is generally less straightforward to be tuned in MMFs. Hence, MCFs are considered to be the preferred medium for long-haul communications given their potential for smaller digital signal processing (DSP) complexity thanks to a generally lower delay spread, when compared to MMFs with same number of modes [12], [3], [10].

In addition, MMF-based SDM systems tend to have a stronger frequency-dependence in the delay spread, higher mode-averaged attenuation and mode-dependent losses, due to stronger Rayleigh scattering (because of the core's doping) [1], [12], [13].

However, several MMF system architectures have been under investigation to reduce the delay spread, from optimized fiber designs [13], [14], to the introduction of intentional coupling through, e.g., spinning during the manufacturing process [15], to the use of gratings as mode couplers [4], [5], [6] or of cyclic modal permutation [5], [16], or fiber spans with different sign of modal delay [5], [1]. More importantly, MMFs can potentially achieve a higher spatial-spectral efficiency than that of MCFs, given their ability to support a larger number of spatial paths [13], [17] in the same cross-sectional area of a single mode fiber (SMF), even above 1000, which had been speculated to be potentially needed by 2035 [18]. This is a strong motivation for investigating MMFs for long distances and, thus, for bringing into play the Kerr nonlinear response of silica fibers.

Kerr nonlinearity depends on the matrix of nonlinear coupling coefficients $\gamma\boldsymbol{\kappa}$, which in the SCR reduces to the scalar $\gamma\kappa$ which is sometimes assumed to scale as $1/M$, where M is the total number of modes [19]. In such a case, under certain conditions, spectral efficiency per mode would increase with M [19]. However, as we showed in [20], the $1/M$ scaling of $\gamma\kappa$ is valid only for a particular fiber design strategy, that is by increasing only the core radius.

In this paper we extend the study of [20] by providing the analytic derivation of an approximate closed-form expression for $\gamma\kappa$ for both the SCR and the IMGCR for different GIMMF design approaches. The analytic results require significantly lower computational time than the current numerical approach, and clarify the relation between $\gamma\boldsymbol{\kappa}$ and the fiber design parameters. Furthermore, they free researchers who deal with, e.g., the development of models for the nonlinear SDM channel, like in [21], [22], [23], from the task of choosing a specific fiber design and computing (or assuming) some values for $\gamma\boldsymbol{\kappa}$.

The work of Paolo Carniello was financially supported by the Federal Ministry of Education and Research of Germany in the program of "Souverän. Digital. Vernetzt.". Joint project 6G-life, project identification number: 16KISK002. The work of Filipe M. Ferreira was financially supported by a UKRI Future Leaders Fellowship [grant number MR/T041218/1].

Paolo Carniello and Norbert Hanik are with the Insitute for Communications Engineering, Technische Universität München, Germany (email: paolo.carniello@tum.de).

Filipe M. Ferreira is with the Optical Networks Group, Dept. Electronic and Electrical Eng., University College London, U.K..

However, the analytic formulas we derive hold formally only for a trenchless GIMMF with parabolic grading, even though some consideration about the validity of the present results to realistic fiber designs are provided in Section V. A relevant contribution is the discovery that the scaling of the nonlinear coefficient $\boldsymbol{\kappa}$ does not depend on the design parameters, but only on the number of guided modes. Hence, to minimize $\gamma\boldsymbol{\kappa}$ it is enough to maximize the fundamental mode effective area. We compare also our numerical and analytic results to values of nonlinear coefficients computed for other optimized fibers proposed in the literature, showing agreement with our framework. We indicate the impact of our analysis to the rates achievable in MMF-based SDM systems. Some considerations for step-index multimode fibers (SIMMFs) are also provided.

The paper is organized as follows. Section II reviews the channel models for the SCR and IMGCR. Section III reviews the basics of fiber design. Section IV presents the main numerical and analytic results about the nonlinear coupling coefficients. Section V places relevant fibers described in the literature within our framework. Section VI explains the implication of this study on the achievable data rates for a simple SDM scenario. Section VII collects some side remarks. Section VIII concludes the paper.

II. Basics of Channel Modeling

A common nonlinear propagation equation for the SCR is the following Manakov equation [24], [19]

$$\frac{\partial \boldsymbol{A}}{\partial z} = \mathrm{L}\left[\boldsymbol{A}\right] - \mathrm{j}\gamma\kappa\|\boldsymbol{A}\|^2\boldsymbol{A} \tag{1}$$

where $\boldsymbol{A} = [A_1, \ldots, A_M]^{\mathrm{T}}$ is the column vector of modal envelopes (T is the transpose operator), M is the total number of modes (i.e., including polarizations), and $\mathrm{L}\left[\boldsymbol{A}\right]$ is the linear operator accounting for all linear effects, in particular strong mode-coupling and dispersion. The last term of Eq. (1) is Kerr nonlinear effect, which depends on two coefficients that in the weak-guidance approximation (which is commonly assumed to hold for fibers for modern optical communications [25]) can be computed as [19]

$$\gamma = \frac{\omega_0 n_2}{c\mathcal{A}_{11}} \tag{2}$$

$$\kappa = \frac{4}{3}\frac{2N}{2N+1}\frac{\mathcal{A}_{11}}{N^2}\sum_{a=1}^{N}\sum_{b=1}^{N}\frac{1}{\mathcal{A}_{ab}} \tag{3}$$

where N is the number of spatial modes (so that $N = M/2$), and

$$\mathcal{A}_{ab} = \frac{\int_{-\infty}^{\infty}\int_{-\infty}^{\infty}|\boldsymbol{F}_a|^2\,\mathrm{d}x\,\mathrm{d}y\int_{-\infty}^{\infty}\int_{-\infty}^{\infty}|\boldsymbol{F}_b|^2\,\mathrm{d}x\,\mathrm{d}y}{\int_{-\infty}^{\infty}\int_{-\infty}^{\infty}|\boldsymbol{F}_a|^2|\boldsymbol{F}_b|^2\,\mathrm{d}x\,\mathrm{d}y} \tag{4}$$

is the intermodal effective area between spatial modes $\boldsymbol{F}_a$ and $\boldsymbol{F}_b$ [19, Eq.60]. The working wavelength is $\lambda_0 = 1550\,\mathrm{nm}$, $\omega_0 = 2\pi c/\lambda_0$ is the working angular frequency, $k_0 = \frac{2\pi}{\lambda_0}$ is the wavenumber in vacuum, the nonlinear refractive index is $n_2 = 2.6\cdot 10^{-20}\,\mathrm{m^2W^{-1}}$, and c is the light-speed in vacuum.

For the IMGCR, a common nonlinear propagation equation is the following Manakov equation [19, Eq.54]

$$\frac{\partial \boldsymbol{A}_a}{\partial z} = \mathrm{L}\left[\boldsymbol{A}_a\right] - \mathrm{j}\gamma\sum_{b=1}^{M_{\mathrm{g}}}\kappa_{ab}\|\boldsymbol{A}_b\|^2\boldsymbol{A}_a \tag{5}$$

where $\boldsymbol{A}_a$ is the N_a-dimensional vector obtained by stacking only the modal amplitudes of the a-th modal group, N_x is the number of spatial modes of the x-th modal-group, M_{g} is the total number of modal groups, and this time $\mathrm{L}\left[\boldsymbol{A}\right]$ accounts for the linear effects of the IMGCR. Note that, conversely to Eq. (1), Eq. (5) contains multiple nonlinear coupling coefficients, which in the weak-guidance can be computed as [19, Eq.61-63]

$$\kappa_{ab} = \frac{4}{3}\frac{2N_a}{2N_a+\delta_{ab}}\frac{\mathcal{A}_{11}}{\bar{\mathcal{A}}_{ab}} \tag{6}$$

where $\delta_{ab} = \begin{cases} 1 & \text{if } a = b \\ 0 & \text{if } a \neq b \end{cases}$ is the Kronecker's delta, and

$$\bar{\mathcal{A}}_{ab} = \left(\frac{1}{2N_a 2N_b}\sum_{\alpha\in I_a}\sum_{\beta\in I_b}\frac{1}{\mathcal{A}_{\alpha\beta}}\right)^{-1} \tag{7}$$

with I_x being the set of indices of the modes (including polarizations) which belong to group x. Note that the various κ_{ab} can be grouped in the matrix $\boldsymbol{\kappa}$. In case of a single group of degenerate modes, Eq. (6) reduces to Eq. (3).

As a side remark, some MMF systems might not strictly operate in either of the two considered regimes, SCR and IMGCR, but rather in an intermediate coupling regime [26], [27], [28], whose study is however outside the scope of this paper.

Throughout the paper we present and compare three methods for computing nonlinear coupling coefficients. The first method consists in numerically computing the modal profiles for the fiber geometry of interest with a mode solver, and then carrying out the numerical integration of Eq. (4) to get $\boldsymbol{\kappa}$ with Eq. (6). The second method consists in exploiting an analytic closed-form expression for Eq. (6) derived later in this work. The third method consists in fitting the results obtained with the first one. In the following we will refer to the first method as the exact numerical method, to the second as the analytic method, and to the third as the fitted formula.

III. Basics of Fiber Design

Designing a MMF essentially consists in selecting the refractive index profile $n(\rho)$ of the fiber, where ρ is the radial coordinate. Common profiles, that are the ones which we consider, are the parabolic graded-index (GI) and the step-index (SI), which are defined respectively as [29, Eq.2.78]

$$n_{\mathrm{GI}}(\rho) = \begin{cases} n_{\mathrm{core}}\sqrt{1-2\Delta\left(\frac{\rho}{R}\right)^2}, & \text{if } \rho \leq R \\ n_{\mathrm{core}}\sqrt{1-2\Delta}, & \text{if } \rho > R \end{cases} \tag{8}$$

and

$$n_{\mathrm{SI}}(\rho) = \begin{cases} n_{\mathrm{core}}, & \text{if } \rho \leq R \\ n_{\mathrm{clad}}, & \text{if } \rho > R \end{cases} \tag{9}$$

where $\Delta = (n_{\mathrm{core}}^2 - n_{\mathrm{clad}}^2)/(2n_{\mathrm{core}}^2)$ is the refractive index difference, n_{core} is the maximum value of $n(\rho)$ in the core, n_{clad} is the constant value of $n(\rho)$ in the cladding, and R is the core radius.

In case advanced refractive index profiles (like the non-parabolic graded-index) or trenches were employed, which is not done here, few more geometrical parameters would

have to be taken into account. Some considerations about the extension of the presented results to non-parabolic GI profiles with trenches are given in Section V.

The total number of guided modes M depends on $n(\rho)$ and on the normalized frequency $V = k_0 R \mathrm{NA}$, where $\mathrm{NA} = \sqrt{n_{\mathrm{core}}^2 - n_{\mathrm{clad}}^2}$ is the so-called numerical aperture [29, Eq.2.80]. For a GIMMF, an approximate relation between V and M is [29, Eq.2.81]

$$M \approx \frac{V^2}{4} \tag{10}$$

while for a SIMMF it holds [29, Eq.2.61]

$$M \approx \frac{V^2}{2} \tag{11}$$

Observe that, even though M is formally a positive integer, it will be sometimes treated here as a positive real number for simplicity of notation.

The design of a MMF aims at minimizing several detrimental effects like modal delays, mode-dependent losses, and coupling losses (in particular bend losses) [30], [31], [13], while guiding a specific number of modes. It is known that increasing Δ tends to increase the modal delays, and the mode-averaged and relative Rayleigh scattering of the different modes, which influence the mode-averaged attenuation and the mode-dependent losss (MDLs)[13]. However, a higher Δ better confines the modal profiles, reducing the bend losses [32]. Increasing R is a straightforward approach to increase M, but it is hard to support more than approximately 200 modes without increasing Δ (beyond a conventional $\sim 0.5\%$). Hence, it is in general helpful to tune both R and Δ when designing a fiber for a specific M [30], [13]. As such, it is of interest to study the scaling of $\gamma\boldsymbol{\kappa}$ in the general scenario where both R and Δ are varied.

We set $n_{\mathrm{clad}} \approx 1.444$, as for a pure silica cladding at $1550\,\mathrm{nm}$, for the design of fibers employed later for numerical analysis. Even though the actual fiber material is not relevant for our single-frequency study, in practice values of $n(\rho)$ higher than n_{clad} (e.g., for the core) can be achieved with germanium doping, while lower values (e.g., for trenches) can be obtained with fluorine doping [33].

Given a fiber supporting M modes, it has always been chosen for the numerical results of this paper the highest possible V before reaching the cutoff frequency V_{c} of the subsequent modal group, so that the guided modes exhibit the strongest confinement [34], [30], [13]. All numerical results have been obtained with the linearly polarized (LP) mode solver described in [35], based on [36], and valid under the assumption of weak-guidance. The choice of modal basis is irrelevant for $\gamma\boldsymbol{\kappa}$, as long as the modes of a modal group of a certain basis are obtained through a unitary transformation of (quasi)-degenerate vector modes [37], [38]. The cutoff frequencies V_{c} for the various modes have been computed with the implicit method in [39, Eq.6] for GIMMFs, and as zeros of Bessel functions of the first-kind for SIMMFs [40, p.320], assuming weak-guidance in both cases. For GIMMFs, we considered only fibers supporting $M = M_{\mathrm{g}}(M_{\mathrm{g}}+1)$ modes, where M_{g} is the total number of modal groups, with the generic i-th modal group consisting of $2i$ modes (including polarizations), as customary in the literature.

Table I: Parameters for relevant GIMMFs in Fig.1

M	$\Delta\,(\%)$	$R\,(\mu\mathrm{m})$	$\mathcal{A}_{11}\,(\mu\mathrm{m}^2)$	κ	$\gamma\kappa\,(1/\mathrm{W/km})$
2	0.41	6.6	86	8/9	1.1
2	0.0072	50	4071	8/9	0.023
42	5.0	6.8	21	0.26	1.3
182	0.43	50	574	0.13	0.024
2352	5.0	50	161	0.037	0.024

IV. Scaling of the Nonlinear Coupling Coefficients with Index Difference and Core Radius

We start from the SCR in Section IV-A for which the scalar $\gamma\kappa$ is used, followed by the IMGCR case in Section IV-B for which the matrix $\gamma\boldsymbol{\kappa}$ has to be considered. The analysis is mainly carried out for GIMMFs; some considerations on SIMMFs are provided in Section IV-C.

A. Strong-Coupling Regime

In order to understand the scaling of $\gamma\kappa$ in a generic scenario where both R and Δ are varied, we firstly consider cases in which only one of the two parameters is varied, while the other is held fixed. In doing so, we also find bounds on $\gamma\kappa$, as it will be clear later. In particular, we start from a baseline GIMMF with core radius $R = R_{\mathrm{GISMF}}$ and refractive index $\Delta = \Delta_{\mathrm{GISMF}}$. Then, a first design option is to increase only R from R_{GISMF} to $R_{\max}$ (fixed Δ), and then increase Δ from Δ_{GISMF} to $\Delta_{\max}$ (fixed R). Starting from the same baseline GIMMF, another design option is to increase only Δ from Δ_{GISMF} to $\Delta_{\max}$, and then increase only R from R_{GISMF} up to $R_{\max}$. A final approach, which serves to derive a bound on $\gamma\kappa$ for large mode area fibers (LMAs), consists in starting from a baseline fiber with $R = R_{\max}$ and $\Delta = \Delta_{\min,\mathrm{GI}}$, and then increasing Δ up to $\Delta_{\max}$.

We chose $R_{\mathrm{GISMF}} = 6.6\,\mu\mathrm{m}$ and $\Delta_{\mathrm{GISMF}} = 0.41\%$, so that $\mathcal{A}_{11} \approx 86\,\mu\mathrm{m}^2$, similarly to a standard SMF [41]. We set $\Delta_{\max} = 5\%$, $R_{\max} = 50\,\mu\mathrm{m}$, and $\Delta_{\min,\mathrm{GI}} = 0.0072\%$. Extreme Δ and R values are considered for maximum generalization. A higher $\Delta_{\max}$ would tend to break the weak-guidance approximation, and would not be practical since modal delays and mode-dependent losses would be too high [13]. The value of $R_{\max}$ was bound by fixing a $125\,\mu\mathrm{m}$ diameter cladding as for SMFs for device backward compatibility [42], and mechanical reliability [10], [42], [13].

The results of the approach in terms of $\gamma\kappa$ have been plotted in Fig.1, which presents the bounds and the set of achievable values for $\gamma\kappa$. For convenience these have been summarised in Table I for relevant fibers, with their design parameters.

In the following section we analyse in more detail individual parts of the aforementioned approach, to derive approximate closed-form expressions for γ, κ, and $\gamma\kappa$.

1) Scaling with the Core Radius: To study the dependence of $\gamma\kappa$ on R, we consider the set of GIMMFs with increasing M, obtained by increasing R from R_{GISMF} to $R_{\max}$, while keeping Δ fixed to either $\Delta = \Delta_{\max}$ or $\Delta = \Delta_{\mathrm{GISMF}}$. We recently

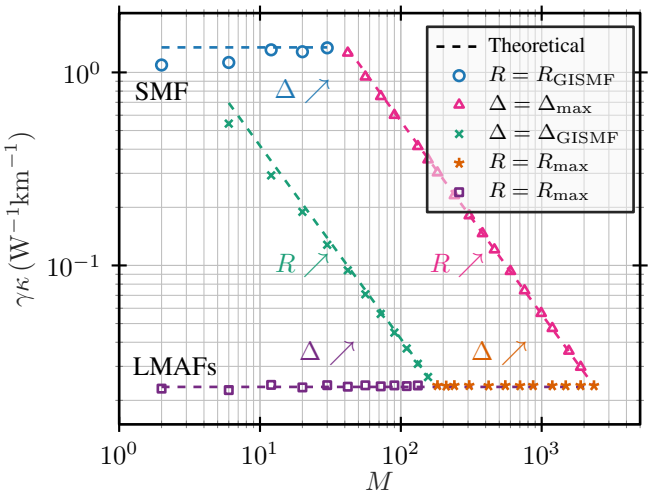

Figure 1: Scaling of $\gamma\kappa$ with M for different GIMMF designs. Markers indicate numerical results with the approach explained in the text. The dashed lines are the proposed theoretical trends: cyan is Eq. (16) with $R = R_{\mathrm{GISMF}}$; magenta is Eq. (14) with $\Delta = \Delta_{\max}$; green is Eq. (14) with $\Delta = \Delta_{\mathrm{GISMF}}$; violet is Eq. (16) with $R = R_{\max}$.

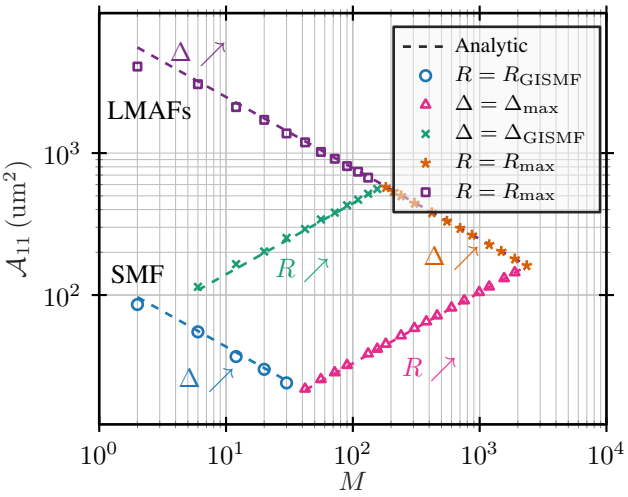

Figure 2: Scaling of $\mathcal{A}_{11}$ with M for different GIMMF designs. Markers indicate numerical results. The dashed lines are the proposed theoretical trends: cyan is Eq. (15) with $R = R_{\mathrm{GISMF}}$; magenta is Eq. (12) with $\Delta = \Delta_{\max}$; green is Eq. (12) with $\Delta = \Delta_{\mathrm{GISMF}}$; violet is Eq. (15) with $R = R_{\max}$.

proposed the following approximate closed-form expressions for the fundamental mode effective area and the Manakov nonlinearity coefficient [20]

$$\mathcal{A}_{11} \approx \pi \frac{1}{(\mathrm{NA}k_0)^2} 4\sqrt{M} \tag{12}$$

$$\kappa \approx \frac{7}{4\sqrt{M}} \tag{13}$$

Eq. (12) has been derived through the Gaussian approximation for the fundamental mode, as detailed in Appendix A. The comparison between the exact numerical result for $\mathcal{A}_{11}$ and the approximate formula Eq. (12) is visible in Fig. 2 for the cases $\Delta = \Delta_{\max}$ and $\Delta = \Delta_{\mathrm{GISMF}}$.

Eq. (13) was obtained in [20] by fitting the exact numerical results, while in Appendix C we derive analytic results for κ, through the infinite parabolic profile approximation. In particular, the analytic derivation yields the values of κ reported in Table II for any GIMMF up to 32 modal groups (1056 modes), regardless of whether R and/or Δ are varied. The agreement between the numerical results and the fitted formula is visible in Fig. 3, for the cases $\Delta = \Delta_{\max}$ and $\Delta = \Delta_{\mathrm{GISMF}}$. The agreement between the numerical and the analytic results is visible in Fig. 4.

Eq. (12) and Eq. (13), with the help of Eq. (2), lead to

$$\gamma\kappa \approx \frac{\omega_0 n_2}{c} \frac{7}{4} \frac{(\mathrm{NA}k_0)^2}{4\pi M} \tag{14}$$

whose agreement with the numerical results is visible in Fig.1, for the cases $\Delta = \Delta_{\max}$ and $\Delta = \Delta_{\mathrm{GISMF}}$.

Observe that due to the approximations involved in obtaining Eq. (14) (in particular due to Eq. (10) and the neglect of the last two terms of Eq. (22) in Appendix A, which are quite rough for M low), the accuracy for $M = 2$, i.e., the SMF case, is quite bad. A better approximation in this case is Eq. (16).

The intuition behind the trend $\gamma\kappa \propto 1/M$ is that two effects act in the same direction. Firstly, the fundamental mode

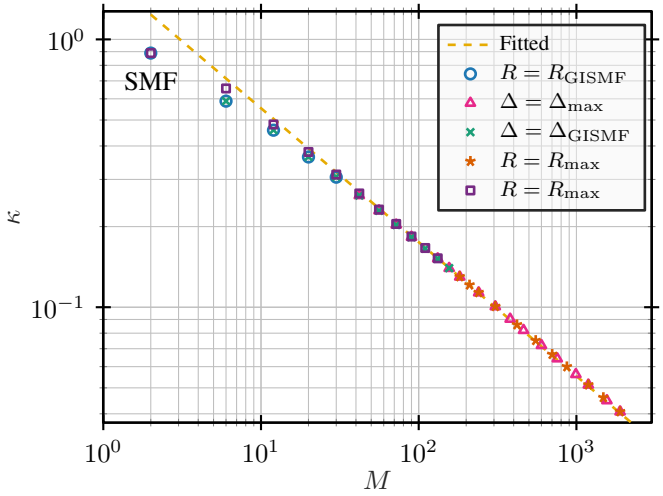

Figure 3: Scaling of κ with M for different GIMMF designs. Markers indicate numerical results. The yellow dashed line is the proposed fitted formula Eq. (13).

effective area $\mathcal{A}_{11}$, which is a measure of how much a mode spreads over a cross-section of the fiber, increases with R. Thus, γ reduces as $1/\mathcal{A}_{11}$, as exemplified by the modal profiles for three different fibers in Fig.5. Secondly, the inclusion of a larger number of modes with a greater effective area $\mathcal{A}_{kk}$ into the averaging procedure to compute κ [19], lowers κ.

2) Scaling with the Index Difference: To study the dependence of $\gamma\kappa$ on Δ, we considered the set of GIMMFs with increasing M, obtained by increasing Δ from Δ_{GISMF} (or from $\Delta_{\mathrm{min,GI}}$) to $\Delta_{\max}$, fixed R. We recently proposed the following approximate closed-form expressions [20]

$$\mathcal{A}_{11} \approx \frac{\pi R^2}{\sqrt{M}} \tag{15}$$

$$\kappa \approx \frac{7}{4\sqrt{M}}$$

Table II: Analytic values of κ for strongly-coupled GIMMFs with increasing number of guided modes.

M	2	6	12	20	30	42	56	72
κ	8/9	40/63	56/117	8/21	88/279	104/387	40/171	136/657
M	90	110	132	156	182	210	240	272
κ	152/819	56/333	184/1197	200/1413	8/61	232/1899	248/2169	88/819
M	306	342	380	420	462	506	552	600
κ	280/2763	296/3087	104/1143	328/3789	344/4167	40/507	376/4977	392/5409
M	650	702	756	812	870	930	992	1056
κ	136/1953	424/6327	440/6813	152/2439	472/7839	488/8379	56/993	520/9513

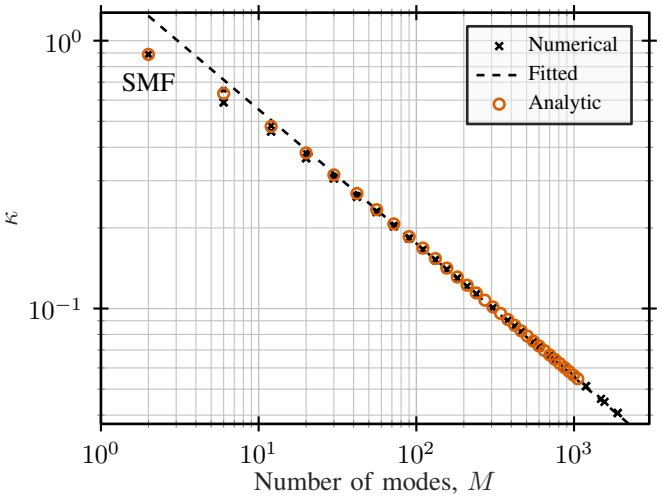

Figure 4: Comparison between the numerical results (crosses, same as Fig. 3), the fitted formula Eq. (13) (dashed line), and the analytic results (circles, from Table II).

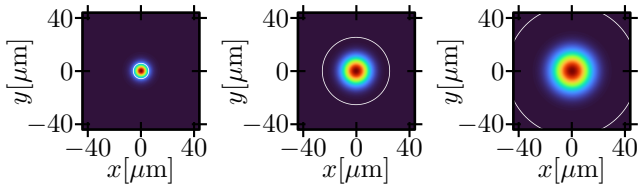

Figure 5: Intensity profiles of the fundamental modes of a set of fibers with increasing R, fixed Δ, and, hence, increasing $\mathcal{A}_{11}$.The white line indicates the core boundary.

The derivation of Eq. (15) follows a similar approach to Eq. (12) and is given in Appendix B. The expression for κ is the same as in Section IV-A1, since, as proved in Appendix C, κ depends on M and not on R or on Δ alone. Hence, the analytic values for κ are again the ones in Table II, displayed in Fig. 4.

The comparison between the exact numerical results and the approximate formulas is visible in Fig. 2 for $\mathcal{A}_{11}$ and in Fig. 3 for κ, for the cases $R = R_{\mathrm{GISMF}}$ and $R = R_{\max}$.

The previous formulas, with the help of Eq. (2), lead to

$$\gamma\kappa \approx \frac{\omega_0 n_2}{c}\frac{7}{4}\frac{1}{\pi R^2} \tag{16}$$

where we stress that all the parameters (including R) are constant in this scenario. The comparison between the numerical results and Eq. (16) is given in Fig.1 for the cases $R = R_{\mathrm{GISMF}}$ and $R = R_{\max}$, where it can be seen that $\gamma\kappa$ remains nearly constant as Δ is scaled.

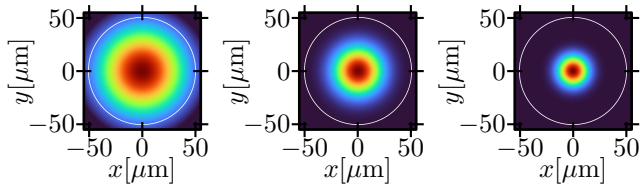

Figure 6: Intensity profiles of the fundamental modes of a set of fibers with increasing Δ, fixed R, and, hence, decreasing $\mathcal{A}_{11}$. The white line indicates the core boundary.

The intuition behind the (quasi-)constant behavior of $\gamma\kappa$ in this scenario is that two effects balance each other out. The first is that $\mathcal{A}_{11}$ reduces with Δ, since the modes are more confined in the core, as exemplified by the modal profiles for three different fibers in Fig.6. Thus, $\gamma \propto 1/\mathcal{A}_{11}$ increases. On the other hand, κ decreases with M for the same qualitative reason as in the previous section.

It is worth mentioning that Eq. (14) and Eq. (16) are in fact valid for any GIMMF, also when both Δ and R are let free. Nevertheless, Eq. (16) is best suited for the case of fixing Δ and varying R, in particular for small M, since its derivation does not involve the approximation Eq. (10). The disadvantage is that the link between $\gamma\kappa$ and M becomes hidden behind R for Eq. (16) and behind NA for Eq. (14), in case both R and Δ are varied together.

Finally, observe from Fig.1 that the scaling of $\gamma\kappa$ with M is not simply $1/M$, but depends on the strategy to increase M – subject to the consideration of the linear effects (e.g., modal dispersion) [30], [13]. The $\gamma\kappa \propto 1/M$ scaling is possible only for $M \lesssim 200$. A design strategy with poor $\gamma\kappa$ roll-off with M, as for fixed R, may lead to enhanced nonlinearities, as discussed in Section VI.

B. Intra-Modal Group Coupling Regime

In the case of the IMGCR, the nonlinear coupling coefficients form a symmetric square matrix $\gamma\boldsymbol{\kappa}$ – whose size matches the number of mode groups. To find a closed-form expression for that, we can approximate again γ and $\boldsymbol{\kappa}$ separately. The γ coefficient can be expressed through Eq. (12)-Eq. (15) as before. In Appendix C we derived the analytic κ_{ab} reported in Table III for a GIMMF up to the first 10 groups (110 polarization modes), regardless of whether R and/or Δ are varied. The analytic κ_{ab} for a GIMMF up to the first 32 groups

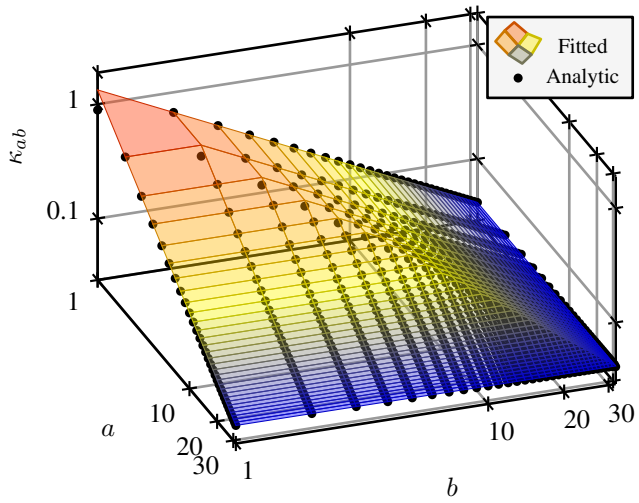

Figure 7: Comparison between the analytic $\boldsymbol{\kappa}$ and the fitted surface Eq. (17) for a GIMMF up to 32 modal groups.

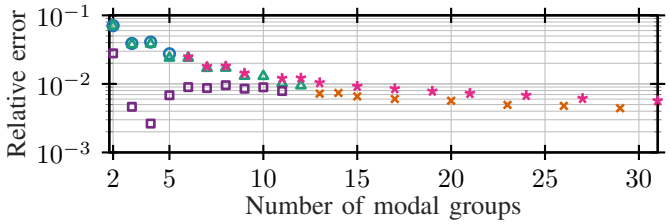

Figure 8: Average absolute relative error between the exact and the analytic $\boldsymbol{\kappa}$ for each GIMMF of Fig. 1 up to 32 groups. The SMF case is not displayed as the error is 0. Markers as in Fig. 1.

(1056 polarization modes) are provided in [43]. In addition, we propose the following simple relation obtained by fitting the exact numerical and the analytic results

$$\kappa_{ab} \approx \frac{4}{3} \cdot \begin{cases} \frac{1}{a}, & \text{if } a < b \\ \frac{1}{b}, & \text{if } a \geq b \end{cases} \tag{17}$$

Fig. 7 displays the analytic result of Table III and the fitted formula Eq. (17). The relative error between the exact and the analytic $\boldsymbol{\kappa}$ for each fiber of Fig. 1 up to 32 groups, computed as average of the absolute element-wise difference between the exact $\boldsymbol{\kappa}$ and the analytic one, is reported in Fig. 8. The average error is around 7% for a 6-modes GIMMFs, and reduces to below 0.5% for a 1056-modes GIMMFs.

Similarly to the case of SCR, the fitted formula is worse for the lower order groups of a certain fiber, and thus also for fibers with few modal groups, as visible in Fig. 7. In particular, for the SMF case, Eq. (13) yields $7/(4\sqrt{2})$ while Eq. (17) yields $4/3$, both being quite far apart with respect to the exact and analytic $8/9$ value.

Finally, observe that within our approximations the $\boldsymbol{\kappa}$ matrices do not depend on the number of fiber modes, such that for any two GIMMFs with M_1 and M_2 modes respectively, and $M_2 > M_1$, $\boldsymbol{\kappa}$ for the M_1-modes fiber is a submatrix of the $\boldsymbol{\kappa}$ for the M_2-modes fiber. Hence, the data in Table III are valid for the κ_{ab} of the first 10 modal groups of any GIMMF, and the ones in [43] for the first 32 modal groups.

Table III: Analytic values of κ_{ab} for a GIMMF up to 10 modal groups. The analytic κ_{ab} for a GIMMF up to the first 32 groups (1056 modes) are provided in [43].

a \ b	1	2	3	4	5	6	7	8	9	10
1	$\frac{8}{9}$	$\frac{2}{3}$	$\frac{4}{9}$	$\frac{1}{3}$	$\frac{4}{15}$	$\frac{2}{9}$	$\frac{4}{21}$	$\frac{1}{6}$	$\frac{4}{27}$	$\frac{2}{15}$
2	$\frac{2}{3}$	$\frac{8}{15}$	$\frac{4}{9}$	$\frac{1}{3}$	$\frac{4}{15}$	$\frac{2}{9}$	$\frac{4}{21}$	$\frac{1}{6}$	$\frac{4}{27}$	$\frac{2}{15}$
3	$\frac{4}{9}$	$\frac{4}{9}$	$\frac{8}{21}$	$\frac{1}{3}$	$\frac{4}{15}$	$\frac{2}{9}$	$\frac{4}{21}$	$\frac{1}{6}$	$\frac{4}{27}$	$\frac{2}{15}$
4	$\frac{1}{3}$	$\frac{1}{3}$	$\frac{1}{3}$	$\frac{8}{27}$	$\frac{4}{15}$	$\frac{2}{9}$	$\frac{4}{21}$	$\frac{1}{6}$	$\frac{4}{27}$	$\frac{2}{15}$
5	$\frac{4}{15}$	$\frac{4}{15}$	$\frac{4}{15}$	$\frac{4}{15}$	$\frac{8}{33}$	$\frac{2}{9}$	$\frac{4}{21}$	$\frac{1}{6}$	$\frac{4}{27}$	$\frac{2}{15}$
6	$\frac{2}{9}$	$\frac{2}{9}$	$\frac{2}{9}$	$\frac{2}{9}$	$\frac{2}{9}$	$\frac{8}{39}$	$\frac{4}{21}$	$\frac{1}{6}$	$\frac{4}{27}$	$\frac{2}{15}$
7	$\frac{4}{21}$	$\frac{4}{21}$	$\frac{4}{21}$	$\frac{4}{21}$	$\frac{4}{21}$	$\frac{4}{21}$	$\frac{8}{45}$	$\frac{1}{6}$	$\frac{4}{27}$	$\frac{2}{15}$
8	$\frac{1}{6}$	$\frac{1}{6}$	$\frac{1}{6}$	$\frac{1}{6}$	$\frac{1}{6}$	$\frac{1}{6}$	$\frac{1}{6}$	$\frac{8}{51}$	$\frac{4}{27}$	$\frac{2}{15}$
9	$\frac{4}{27}$	$\frac{4}{27}$	$\frac{4}{27}$	$\frac{4}{27}$	$\frac{4}{27}$	$\frac{4}{27}$	$\frac{4}{27}$	$\frac{4}{27}$	$\frac{8}{57}$	$\frac{2}{15}$
10	$\frac{2}{15}$	$\frac{2}{15}$	$\frac{2}{15}$	$\frac{2}{15}$	$\frac{2}{15}$	$\frac{2}{15}$	$\frac{2}{15}$	$\frac{2}{15}$	$\frac{2}{15}$	$\frac{8}{63}$

C. Step-Index Fibers

Even though employing SIMMFs for long-haul communications might be even more challenging than utilizing GIMMFs due to a larger delay spread [10] and a non-uniform spacing of cutoff frequencies, scaling trends are derived here for the sake of completeness.

The same approach as the one devised to study GIMMFs is employed here for SIMMFs. The chosen starting point is a fiber with $R_{\text{SISMF}} = 4.1\,\mu\text{m}$ and $\Delta_{\text{SISMF}} = 0.32\%$, to mimic a SSMF with $\mathcal{A}_{11} = 85\,\mu\text{m}$ [41]. The other relevant parameters are $R_{\max} = 50\,\mu\text{m}$, $\Delta_{\min,\text{SI}} = 0.0034\%$, and $\Delta_{\max} = 5\%$. In Fig. 9, the exact numerical results and the respective fitting is shown for SIMMFs. From the figure, it still holds that

$$\gamma\kappa \propto \begin{cases} 1/M, & \text{if } R \text{ is varied fixed } \Delta \\ \text{const}, & \text{if } \Delta \text{ is varied fixed } R \end{cases} \tag{18}$$

but with less accuracy than for GIMMFs. The scaling of $\mathcal{A}_{11}$ and κ with number of modes when varying R and Δ is displayed in Fig. 10 and in Fig. 11, including the semi-analytic approximation of $\mathcal{A}_{11}$ reported in Appendix E. Given the lower interest in SIMMFs for long-haul communications compared to GIMMFs, we do not provide an analytic result for κ, even though a more quantitative discussion is carried out in Appendix E.

V. Optimized and Manufactured Fibers

In Fig. 12 the $\gamma\kappa$ values for different optimized and/or manufactured GIMMFs described in the literature have been reported against the developed framework, assuming to operate in the SCR. Such fibers have been emulated based on the available information in the respective references, which did not always include all the necessary data about the refractive index profile. Hence, some little discrepancies between the actual $\gamma\kappa$ and the one computed by us are possible.

Nevertheless, the consistency between the $\gamma\kappa$ computed for the fibers in the literature and our framework supports the validity of our investigation. In particular, the optimized fibers lie within the foreseen boundaries, and the approximate trends

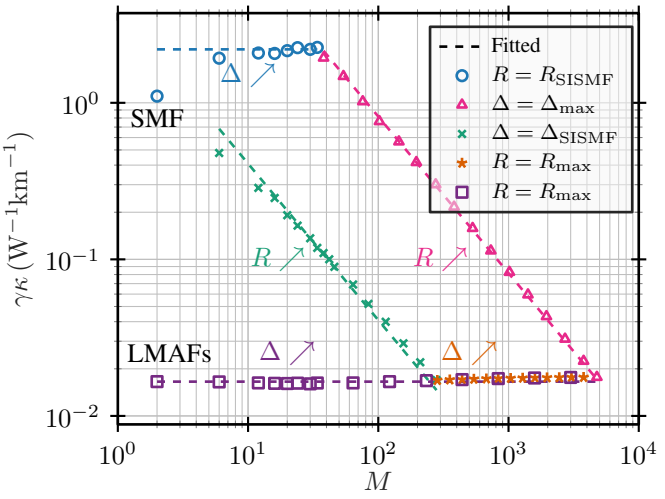

Figure 9: Scaling of $\gamma\kappa$ with M for different SIMMF designs. Markers indicate numerical results. The dashed lines are the trends in Eq. (18) with fitted prefactors.

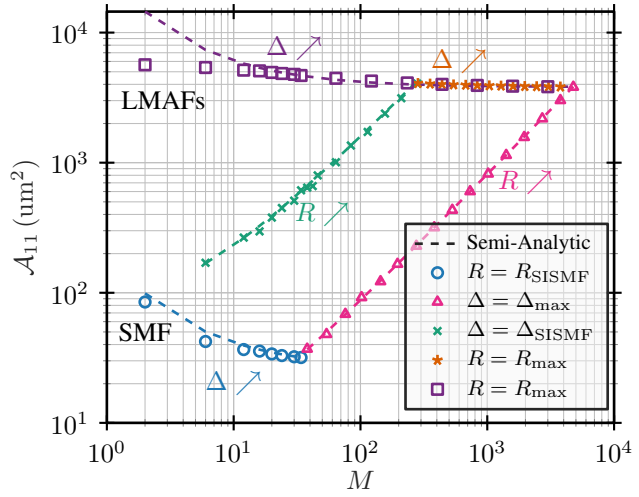

Figure 10: Scaling of $\mathcal{A}_{11}$ with M for different SIMMF designs. Markers indicate numerical results. The dashed lines are the theoretical trends (but with different scaling factors!): cyan is Eq. (58) with $R = R_{\mathrm{SISMF}}$; magenta is Eq. (57) with $\Delta = \Delta_{\max}$; green is Eq. (57) with $\Delta = \Delta_{\mathrm{SISMF}}$; violet is Eq. (58) with $R = R_{\max}$.

for $\gamma\kappa$ ($\propto 1/M$ with R, and const with Δ), are verified again. Similar considerations hold for $\mathcal{A}_{11}$ and κ.

It should be noted that the optimized and manufactured fibers in general exploit more advanced index profiles, which would formally require an extension to the analysis in this paper for a proper comparison. At the same time, we verified that the κ computed (through the exact numerical method) for the literature fibers, which exploit trenches and grading indices slightly different from 2, are close to the κ of the trenchless parabolic GIMMFs. In addition, a quantitative reasoning based on the Gaussian approximation for the effective area of a generic GI profile suggests that for realistic slightly non-parabolic GIs $\gamma\kappa$ deviates by at most 10% from the parabolic case, see Appendix F.

The fiber data used for the plots of the paper, including the fibers emulated from the literature, and additional data like the intermodal effective areas $\mathcal{A}_{ab}$ have been provided in [43].

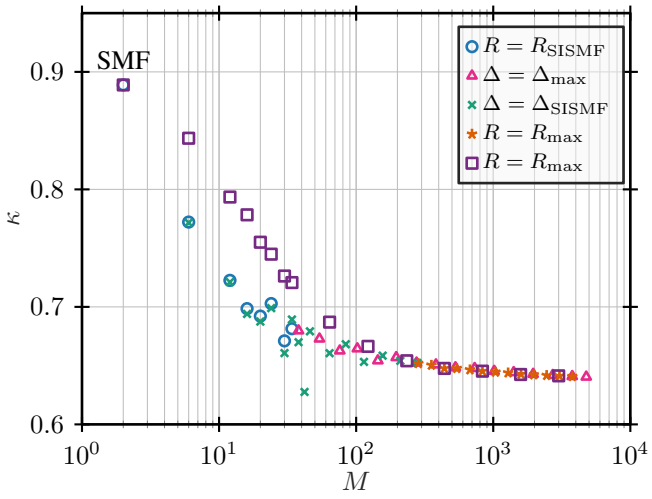

Figure 11: Scaling of κ with M for different SIMMF designs.

VI. Considerations on Data Rates

The ultimate throughput limit of an SDM system in the SCR depends on Kerr nonlinearity, which depends also on $\gamma\kappa$. In order to study the impact of the scaling of $\gamma\kappa$ with M on the data rates of GIMMF systems, let us consider the perturbation model developed in [23]. The model assumes a strongly-coupled SDM fiber with only mode-independent chromatic-dispersion (CD) and Kerr nonlinearity as distortions. No other linear effects like modal delay or MDL are included. Ideal distributed amplification able to perfectly compensate the fiber loss is assumed. Circularly-symmetric complex Gaussian modulation is considered. Digital back-propagation is potentially applied on the channel under test, so that CD and self-phase modulation (SPM) are removed. The mean phase noise is also removed. In such case, the achievable information rate in terms of $\mathrm{bit/s/Hz/mode}$ for an additive white Gaussian noise (AWGN) receiver can be computed as

$$R(M,P) = \log_2\left(1 + \frac{P}{\frac{N_{\mathrm{ASE}}}{T} + \sigma^2_{\mathrm{NLI}}}\right) \tag{19}$$

where P is the transmit power per channel per mode, N_{ASE} is the amplified spontaneous emission (ASE) noise flat power spectral density (PSD) over a band $B = 1/T$, T is the symbol time, and σ^2_{NLI} is the variance of the equivalent nonlinear interference noise. It holds $\sigma^2_{\mathrm{NLI}} = (\gamma\kappa)^2\left(\eta_2 M^2 + \eta_1 M + \eta_0\right)P^3$, where η_x for $x \in \{0,1,2\}$ are coefficients whose computation is described in [23].

Neglecting η_2 (realistic for $M \leq 1000$) and η_0 (rendered negligible for $M > 10$ since $\eta_0 = \eta_1$ in our setup [23]), and fixing the power per mode P, it follows that the scaling of the nonlinear interference σ^2_{NLI}, and thus of the data rate per mode, depends on $(\gamma\kappa)^2 \cdot (\eta_1 M)$. In particular, if $\gamma\kappa$ scales with number of modes faster than $1/\sqrt{M}$, the data rate increases with the number of modes. This would imply that a MMF could achieve a higher data rate than a bundle of SMFs with same total number of modes, fixed the same power per mode. This

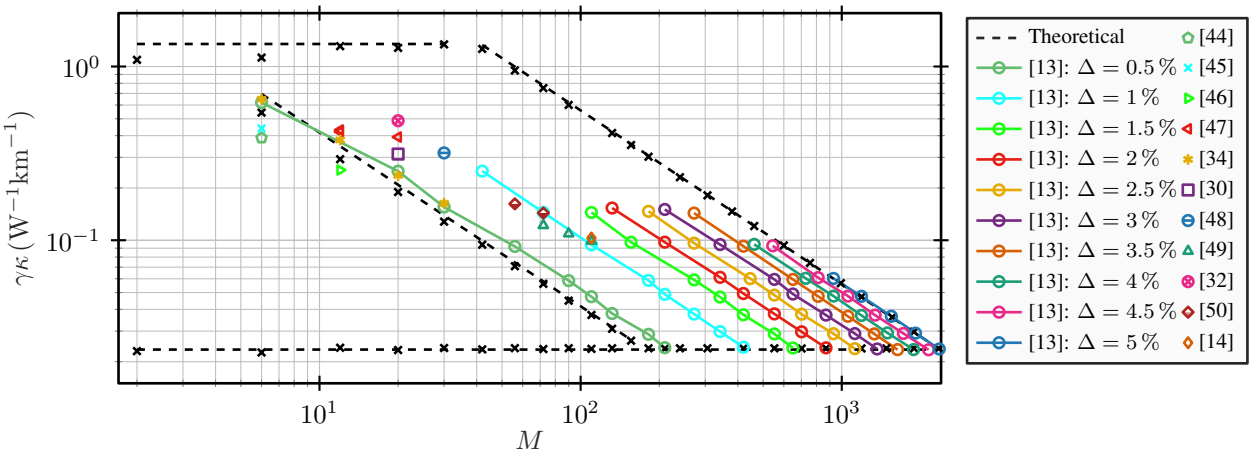

Figure 12: Scaling of $\gamma\kappa$ with M for a number of optimized and manufactured GIMMFs. In black the same lines and points as in Fig. 1.

is depicted in Fig. 13 for a) the best-case scenario $\gamma\kappa = 1/M$ and for b) the (approximate) limiting one $\gamma\kappa = 1/\sqrt{M}$; η_0 and η_2 were not neglected in Fig. 13, and the parameter setup of [23, Table I-II] was used. The different data rate scaling trends in Fig. 13a and Fig. 13b highlights the importance of designing a fiber keeping into account nonlinearity and, hence, $\gamma\kappa$. Note that similar conclusions could be reached with other perturbation models in the literature like the ones in [19], [21].

It is worth mentioning that SDM systems are investigated in the literature for very different transmission scenarios which might not correspond to the one presented in this section. In particular, the data rate per mode with fixed the power per mode might not be the relevant metric in all situations. Thus, the example discussed above is meant as an application of the $\gamma\kappa$ study rather than a general statement on the usefulness of SDM systems.

VII. Side Remarks on Weak-Guidance

Since the weak-guidance approximation for which LP modes exist is typically assumed in the literature for fibers with $\Delta < 1\%$ [36, p.38] [40, p.20], it might have been the case that such approximation did not hold for the MMFs considered in this paper for which $\Delta \in [1\%, 5\%]$. Thus, the accuracy of the numerical results has been checked for some points of Fig.1, including some for which $\Delta = 5\%$, generating the vector-modal profiles with the mode solver described in [35] based on [51]. For the fibers we tested, we observed a maximum discrepancy between the elements of $\boldsymbol{\kappa}$ computed with a scalar and with a vector mode solver below 2% (and much lower in terms of κ in the SCR), justifying the adoption of the scalar solver, which is computationally less expensive. The number of guided modes for each generated fiber in the weak-guidance has also been compared against the number of guided vector-modes without such assumption [52], finding negligible discrepancies.

VIII. Conclusions

We have investigated the scaling of the nonlinear coupling coefficients $\gamma\kappa$ and $\gamma\boldsymbol{\kappa}$, appearing in the Manakov equations for the SCR and the IMGCR, respectively, with the number of modes M supported by GIMMFs and SIMMFs. Analytic expressions have been derived and validated against numerical results, and provide a significantly quicker tool to compute $\gamma\kappa$ and $\gamma\boldsymbol{\kappa}$. Our analysis also indicates that $\boldsymbol{\kappa}$ is approximately independent on the fiber design parameters R and Δ, but it depends only on the number of guided modes. Thus, maximizing the fundamental mode effective area minimizes the elements of $\boldsymbol{\kappa}$. Values of nonlinear coupling coefficients have been computed for optimized and manufactured GIMMFs in the literature and placed within the developed framework.

Our analytic expressions can be used, e.g., in nonlinear SDM channel models [21], [22], [23]. Thus, contributing towards the assessment of the feasibility of a future long-haul SDM communication system.

Appendix A
Closed-Form Expression for the Fundamental Effective Area of GIMMFs: Varying the Core Radius

In order to obtain an approximate analytic expression for $\mathcal{A}_{11}$ when varying only R, let the fundamental mode be approximated with a Gaussian function as [40, Eq.15-2] [53, Eq.2.2.38] [29, Eq.2.74]

$$c \cdot \exp\left(\frac{\rho}{r_0}\right)^2 \tag{20}$$

where $c \geq 0$ is some scaling factor, ρ is the radial coordinate, r_0 is the so-called spot-size. Then, the fundamental mode effective area becomes [53, p.32]

$$\mathcal{A}_{11} = \pi r_0^2 \tag{21}$$

The parameter r_0 can be related to V through different approaches. An empirically-fitted formula is [54, Eq.11]

$$\frac{r_0}{R} = \frac{A}{\sqrt{V}} + \frac{B}{V^{1.5}} + \frac{C}{V^6} \tag{22}$$

with $A = \sqrt{2}$, $B \approx 0.372$, and $C \approx 26.773$. For the case of a parabolic GIMMF, the last two terms are relevant only for low values of V (and thus M). Hence, we neglect them for the sake of simplicity. A similar relation can be obtained with a variational approach, through which it has been shown that,

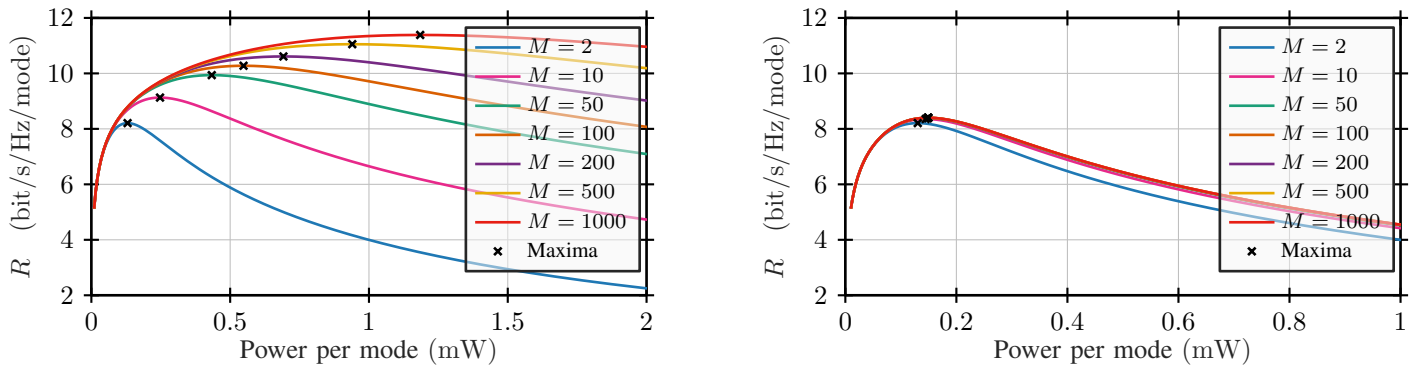

(a) (b)

Figure 13: Comparison between the achievable data rates computed with Eq. (19) when $\gamma\kappa \propto 1/M$ (13a), and when $\gamma\kappa \propto 1/\sqrt{M}$ (13b), within the perturbation model and the assumptions of [23].

for the infinite parabolic refractive index profile, [40, Table 14-2]

$$\frac{r_0}{R} \propto \frac{1}{\sqrt{V}} \tag{23}$$

A similar dependence has been obtained for the Gaussian refractive index profile [40, Table 15-2].

From Eq. (21) and Eq. (22), it turns out that

$$\mathcal{A}_{11} \approx \pi \frac{2R^2}{V} \tag{24}$$

Substituting Eq. (10) in Eq. (24), exploiting the definition of V, and remembering that Δ is fixed (i.e., M changes only because of R), yields

$$\mathcal{A}_{11} \approx \pi \left(\frac{1}{\mathrm{NA}k_0}\right)^2 4\sqrt{M}$$

Appendix B
Closed-Form Expression for the Fundamental Effective Area of GIMMFs: Varying the Refractive Index Difference

The approximate closed formula for $\mathcal{A}_{11}$ when R is fixed can be retrieved with the same Gaussian approach employed in Appendix A. With the help of Eq. (24) and Eq. (10), remembering that this time R is fixed and Δ varies, it is found that

$$\mathcal{A}_{11} \approx \frac{\pi R^2 A^2}{2} \frac{1}{\sqrt{M}}$$

Appendix C
Analytic Expression for the Manakov Nonlinearity Coefficient of GIMMFs

In this section we derive approximate analytic results for the generic nonlinearity coefficient $\kappa_{\alpha\beta}$ of the matrix $\boldsymbol{\kappa}$ for GIMMFs. We remind that $\boldsymbol{\kappa}$ reduces to the scalar κ in case of a single group of strongly-coupled modes.

In order to derive an approximate analytic expression for $\kappa_{\alpha\beta}$ for GIMMFs, the infinite parabolic profile approximation can be exploited, which provides relatively simple analytic expressions for the modal profiles, while for the actual parabolic profile of Eq. (8) the analytic expression would be more complicated, involving the Whittaker functions of the first kind [40, Sec. 14-8]. This approach is commonly employed to obtain closed-form expressions for relevant quantities of GIMMFs like propagation constants and their relative cutoff values [53, Sec.11.2.2], modal profiles, and nonlinear coefficients [55]. The approximation consists in assuming that the refractive index profile is parabolic everywhere, not only in the core. That is, it assumes that Eq. (8) holds also for $\rho > R$. The approximation is reasonable for low-order modes and large enough core radius R [53, Sec.11.2.2], even though we exploit it for all modes and core radii later.

The modal profiles are then [40, Table 14-2][55]

$$\boldsymbol{F}_{p,m}(\rho,\varphi) = \tilde{F}_{p,m}(\rho)\boldsymbol{p}_m(\varphi) \tag{25}$$

where p and m are two integers, ρ is the radial coordinate, φ is the azimuth coordinate, and [55]

$$\tilde{F}_{p,m}(\rho) = A_p^m \frac{\rho^m}{\rho_0^{m+1}} \mathrm{e}^{-\frac{\rho^2}{2\rho_0^2}} L_p^m\left(\frac{\rho^2}{\rho_0^2}\right) \tag{26}$$

where L_p^m is a generalized Laguerre polynomial. The quantity $\tilde{F}_{p,m}(\rho)$ accounts for the radial dependence of the modal profile with

$$A_p^m = \sqrt{\frac{p!}{\pi\,(p+m)!}} \tag{27}$$

$$\rho_0 = \frac{R}{(4N_2)^{1/4}} \tag{28}$$

$$N_2 = \frac{1}{2} n_0^2 k_0^2 R^2 \Delta \tag{29}$$

The coefficient A_p^m has been chosen to fulfill the following orthonormality condition among the modes [55, Eq.5]

$$\int_0^{2\pi}\int_0^{\infty} \rho \boldsymbol{F}^*_{p',m'}(\rho,\varphi)\boldsymbol{F}_{p,m}(\rho,\varphi)\,\mathrm{d}\rho\,\mathrm{d}\varphi = \delta_{p,p'}\delta_{m,m'} \tag{30}$$

The L_p^m are the generalized Laguerre polynomials which can be expressed in different ways. A handy approach for us is [56, Eq.18.59]

$$L_p^m(\rho) = \sum_{i=0}^{n} b_i(n,m)\rho^i \tag{31}$$

where

$$b_i(n,m) = (-1)^i \binom{p+m}{p-i} \frac{1}{i!} \tag{32}$$

With simple algebraic passages it is possible to derive the following expression which can speed up the numerical implementation

$$b_{i+1}(p,m) = -\frac{p-i}{(i+1)(m+i+1)} b_i(p,m) \tag{33}$$

The expression of the polarization and azimuth dependence $\boldsymbol{p}_m(\varphi)$ appearing in Eq. (25) depends on the chosen modal basis. Note that, in case of the LP modes, to draw a link with the classic notation, the mode $\boldsymbol{F}_{p,m}$ corresponds to $\mathrm{LP}_{m,p+1}$[40, p.308]. In case of vector modes, within weak-guidance, the expressions for the polarization vectors $\boldsymbol{p}_m(\varphi)$ are [57, Eq.1]

$$p \geq 0$$
$$\begin{cases} \mathrm{TM}_{0,p+1}(\varphi) = \cos(\varphi)\hat{\boldsymbol{x}} + \sin(\varphi)\hat{\boldsymbol{y}} \\ \mathrm{TE}_{0,p+1}(\varphi) = \sin(\varphi)\hat{\boldsymbol{x}} - \cos(\varphi)\hat{\boldsymbol{y}} \end{cases} \tag{34}$$

$$m > 1, p \geq 0$$
$$\begin{cases} \mathrm{EH}^{\mathrm{e}}_{m-1,p+1}(\varphi) = \cos(m\varphi)\hat{\boldsymbol{x}} + \sin(m\varphi)\hat{\boldsymbol{y}} \\ \mathrm{EH}^{\mathrm{o}}_{m-1,p+1}(\varphi) = \sin(m\varphi)\hat{\boldsymbol{x}} - \cos(m\varphi)\hat{\boldsymbol{y}} \end{cases} \tag{35}$$

$$m \geq 1, p \geq 0$$
$$\begin{cases} \mathrm{HE}^{\mathrm{e}}_{m+1,p+1}(\varphi) = \cos(m\varphi)\hat{\boldsymbol{x}} - \sin(m\varphi)\hat{\boldsymbol{y}} \\ \mathrm{HE}^{\mathrm{o}}_{m+1,p+1}(\varphi) = \sin(m\varphi)\hat{\boldsymbol{x}} + \cos(m\varphi)\hat{\boldsymbol{y}} \end{cases} \tag{36}$$

Note that all modal bases obtained as a unitary transformation of (quasi-)degenerate vector modes lead to the same $\gamma\kappa_{\alpha\beta}$ [37], [38]. Hence, in principle the LP and vector modal basis are equivalent. However, we adopt the vector modes since they simplify the calculations later on.

Starting from Eqs. 6, 4, and 7, the generic nonlinearity coefficient $\kappa_{\alpha\beta}$ can be computed as

$$\kappa_{\alpha\beta} = \frac{4}{3} \frac{1}{(2N_\alpha + \delta_{\alpha,\beta}) 2N_\beta} \sum_{a \in I_\alpha} \sum_{b \in I_\beta} \mathcal{A}_{11} D_{ab} \tag{37}$$

where we exploited the orthonormality so that $\int_{-\infty}^{\infty}\int_{-\infty}^{\infty} \|\boldsymbol{F}_a\|^2 \,\mathrm{d}x\,\mathrm{d}y = \int_{-\infty}^{\infty}\int_{-\infty}^{\infty} \|\boldsymbol{F}_b\|^2 \,\mathrm{d}x\,\mathrm{d}y = 1$, and we defined

$$D_{ab} = \int_0^\infty \int_0^{2\pi} \rho \|\boldsymbol{F}_a\|^2 \|\boldsymbol{F}_b\|^2 \,\mathrm{d}\varphi\,\mathrm{d}\rho \tag{38}$$

where a stands for the pair of modal indices (p,m) and b stands for (s,v). Hence, we now derive a closed-form expression for D_{ab}.

Note that Eq. (6) has been originally derived for LP modes only, while for vector modes a (slightly) more complex expression is normally used [19, Eq.56]. We show in Appendix D that Eq. (6) holds also for vector modes (within weak-guidance) and hence we are allowed to consider Eq. (38) for vector modes as well.[1] Then,

$$\begin{aligned} D_{ab} &= \int_0^\infty \int_0^{2\pi} \rho \|\tilde{F}_{p,m}(\rho)\boldsymbol{p}_m(\varphi)\|^2 \|\tilde{F}_{s,v}(\rho)\boldsymbol{p}_v(\varphi)\|^2 \mathrm{d}\varphi\mathrm{d}\rho \\ &= 2\pi \int_0^\infty \rho \|\tilde{F}_{p,m}(\rho)\|^2 \|\tilde{F}_{s,v}(\rho)\|^2 \,\mathrm{d}\rho \end{aligned} \tag{39}$$

where we made use of $\|\boldsymbol{p}_m(\varphi)\|^2 = \|\boldsymbol{p}_v(\varphi)\|^2 = 1$, thanks to our choice of modal basis.

Substituting Eq. (26) into Eq. (39)

$$\begin{aligned} D_{ab} = \tilde{C}_{ab} \int_0^\infty \rho \rho^{2m+2v} \mathrm{e}^{-2\frac{\rho^2}{\rho_0^2}} L_p^m\left(\frac{\rho^2}{\rho_0^2}\right) \\ L_p^m\left(\frac{\rho^2}{\rho_0^2}\right) L_s^v\left(\frac{\rho^2}{\rho_0^2}\right) L_s^v\left(\frac{\rho^2}{\rho_0^2}\right) \mathrm{d}\rho \end{aligned} \tag{40}$$

where $\tilde{C}_{pmsv} = 2\pi \left(\frac{A_p^m A_s^v}{\rho_0^{m+1}\rho_0^{v+1}}\right)^2$ and $\tilde{C}_{ab}$ is a short-hand notation for $\tilde{C}_{pmsv}$. We perform the change of variable $u = \rho^2$, so that $\mathrm{d}u = 2\rho\,\mathrm{d}\rho$, which yields

$$\begin{aligned} D_{ab} = C_{ab} \int_0^\infty u^{\tau_{mv}} \mathrm{e}^{-\sigma u} L_p^m\left(\frac{u}{\lambda}\right) L_p^m\left(\frac{u}{\lambda}\right) \\ L_s^v\left(\frac{u}{\lambda}\right) L_s^v\left(\frac{u}{\lambda}\right) \mathrm{d}u \end{aligned} \tag{41}$$

where $C_{ab} = \tilde{C}_{ab}/2 = \pi \left(\frac{A_p^m A_s^v}{\rho_0^{m+v+2}}\right)^2$, $\tau_{mv} = m+v$, $\sigma = \rho_0^2/2$, and $\lambda = \rho_0^2$. We now follow similar steps to [58] to retrieve a closed-form expression for the previous formula. Plugging Eq. (31) into Eq. (41), it is obtained

$$\begin{aligned} D_{ab} = C_{ab} \sum_{i=0}^{p}\sum_{j=0}^{p}\sum_{k=0}^{s}\sum_{l=0}^{s} b_i(p,m) b_j(p,m) \\ b_k(s,v) b_l(s,v) \lambda^{\varepsilon-\tau_{mv}} \int_0^\infty \mathrm{e}^{-\sigma u} u^\varepsilon \,\mathrm{d}u \end{aligned} \tag{42}$$

where $\varepsilon = i+j+k+l+\tau_{mv}$. With the change of variable $x = \sigma u$, the integral $\int_0^\infty \mathrm{e}^{-\sigma u} u^\varepsilon \,\mathrm{d}u$ becomes

$$\sigma^{-(\varepsilon+1)} \int_0^\infty \mathrm{e}^{-x} x^\varepsilon \,\mathrm{d}x = \sigma^{-\varepsilon+1}\Gamma(\varepsilon+1) = \sigma^{-(\varepsilon+1)}\varepsilon! \tag{43}$$

where the last passage holds only for integer values of ε, and where $\Gamma(\varepsilon+1) = \int_0^\infty \mathrm{e}^{-x} x^\varepsilon \,\mathrm{d}x$ is the well-known gamma function. Observe also that $C_{ab}\lambda^{\varepsilon-\tau_{mv}}\sigma^{-(\varepsilon+1)} = C_{ab}\frac{\rho_0^{2(1+\tau_{mv})}}{2^{\varepsilon+1}} = \frac{\left(A_p^m A_s^v\right)^2}{\rho_0^2 2^{\varepsilon+1}}$. Then, Eq. (42) becomes

$$D_{ab} = \frac{\left(A_p^m A_s^v\right)^2}{\rho_0^2} \tilde{D}_{ab} \tag{44}$$

where

$$\tilde{D}_{ab} = \sum_{i=0}^{p}\sum_{j=0}^{p}\sum_{k=0}^{s}\sum_{l=0}^{s} b_i(p,m) b_j(p,m) b_k(s,v) b_l(s,v) \frac{\varepsilon!}{2^{\varepsilon+1}} \tag{45}$$

[1] Since employing vector modes, it is enough to account for one mode per LP group, where an LP group consists of either 2 modes (for the LP_{0x} modes (with $x \in \{1,2,\dots\}$)), or 4 modes. Indeed, D_{ab} depends only on the norm of the modes, which is the same for all vector modes within the same LP modal group (while this is not the case for the LP modes of a certain LP modal group). Hence, the later symbolic calculations are speeded up. Note that when only one vector mode per LP mode is employed, a suitable scaling factor within the summation of (37) is needed.

Inserting Eq. (44) in Eq. (37), we obtain

$$\kappa_{\alpha\beta} = \frac{4\pi}{3} \frac{1}{(2N_a + \delta_{ab})N_b} \sum_{a\in I_\alpha} \sum_{b\in I_\beta} \left(A_p^m A_s^v\right)^2 \tilde{D}_{ab} \quad (46)$$

where we used $\mathcal{A}_{11} = 2\pi\rho_0^2$ [55].

Notice from Eq. (46) that $\kappa_{\alpha\beta}$ does not depend on R or Δ, but just on the number of modes, and it is expressed only in terms of ratios of integers. Hence, $\kappa_{\alpha\beta}$ can be computed exactly (within the infinite parabolic approximation) with, e.g., the help of a software with symbolic computation capabilities, as we did. To know which set of modal indices I_α corresponds to a certain modal group, the approach in [39] is helpful. The analytic values of κ in the SCR for up to 32 modal groups are reported in Table II. For the IMGCR the analytic values are reported in Table III for up to 10 modal groups (110 modes), and in [43] for up to 32 modal groups (1056 modes).

Appendix D
Intermodal Effective Area for Vector Modes

In this section we prove the claim made in Appendix C that Eq. (6) holds not only for the LP modal basis as per [19], but for vector modes 34-36 as well. For a generic basis of real modes in the weakly guiding regime, the nonlinear coupling coefficients $\gamma\kappa_{ab}$ can be computed as [19, Eq.55]

$$\gamma\kappa_{\alpha\beta} = \frac{\omega_0 n_2}{cZ_0^2} \frac{1}{(M_\alpha + \delta_{\alpha\beta})M_\beta} \sum_{a\in I_\alpha} \sum_{b\in I_\beta} \frac{n_{\text{eff}}^2}{N_a^2 N_b^2} I_{ab} \quad (47)$$

where

$$I_{ab} = \frac{1}{6} \int_{-\infty}^{\infty}\int_{-\infty}^{\infty} \|\boldsymbol{F}_a\|^2\|\boldsymbol{F}_b\|^2 + 2\|\boldsymbol{F}_a \cdot \boldsymbol{F}_b\|^2 \,\mathrm{d}x\,\mathrm{d}y \quad (48)$$

Consider two pairs of modes $\{\boldsymbol{F}_a, \boldsymbol{F}_{a'}\}$ with polarizations $\{\boldsymbol{p}_a(\varphi), \boldsymbol{p}_{a'}(\varphi)\}$ (where $\boldsymbol{p}_a(\varphi)$ is orthogonal to $\boldsymbol{p}_{a'}(\varphi)$), and $\{\boldsymbol{F}_b, \boldsymbol{F}_{b'}\}$ with polarizations $\{\boldsymbol{p}_b(\varphi), \boldsymbol{p}_{b'}(\varphi)\}$ (where $\boldsymbol{p}_b(\varphi)$ is orthogonal to $\boldsymbol{p}_{b'}(\varphi)$). In order to obtain Eq. (6) from Eq. (47), we need to prove that [19, Eq.57]

$$I_{ab} + I_{a'b} + I_{ab'} + I_{a'b'} = \frac{4}{3} \int_{-\infty}^{\infty}\int_{-\infty}^{\infty} \|\boldsymbol{F}_a\|^2\|\boldsymbol{F}_b\|^2 \,\mathrm{d}x\,\mathrm{d}y \quad (49)$$

To do so, it is enough to show that

$$I_{2,ab} = I_{1,ab}/2 \quad (50)$$

$\forall\{n, h\}$, where

$$I_{1,ab} = \int_{-\infty}^{\infty}\int_{-\infty}^{\infty} \|\boldsymbol{F}_a\|^2\|\boldsymbol{F}_b\|^2 \,\mathrm{d}x\,\mathrm{d}y \quad (51)$$

and

$$I_{1,ab} = \int_{-\infty}^{\infty}\int_{-\infty}^{\infty} \|\boldsymbol{F}_a \cdot \boldsymbol{F}_b\|^2 \,\mathrm{d}x\,\mathrm{d}y \quad (52)$$

Given the separability of the radial and the azimuth dependence, i.e., the radial dependence can be factored out from the previous integrals, in the following we focus only on the azimuth dependence.

Let us consider

$$\boldsymbol{p}_a = \cos(l\varphi)\hat{\boldsymbol{x}} + \sin(l\varphi)\hat{\boldsymbol{y}} \quad (53)$$

$$\boldsymbol{p}_b = \cos(m\varphi)\hat{\boldsymbol{x}} - \sin(m\varphi)\hat{\boldsymbol{y}} \quad (54)$$

which corresponds to the polarizations of $\mathrm{EH}_{l,p}^{\mathrm{e}}$ (and $\mathrm{TM}_{0,p}$) and $\mathrm{HE}_{m,p}^{\mathrm{e}}$, respectively. It immediately follows that $I_{1,ab} = 2\pi$, while

$$\begin{aligned}
I_{2,ab} &= \int_0^{2\pi} \|\boldsymbol{p}_a \cdot \boldsymbol{p}_b\|^2 \,\mathrm{d}\varphi \\
&= \int_0^{2\pi} \left[\cos(l\varphi)\cos(m\varphi) - \sin(l\varphi)\sin(m\varphi)\right]^2 \mathrm{d}\varphi \\
&= \int_0^{2\pi} \Big(\cos(l\varphi)^2\cos(m\varphi)^2 + \sin(l\varphi)^2\sin(m\varphi)^2 \\
&\quad - 2\cos(l\varphi)\sin(l\varphi)\cos(m\varphi)\sin(m\varphi)\Big)\,\mathrm{d}\varphi \\
&= \int_0^{2\pi} \frac{1}{4}(1+\cos(2l\varphi))(1+\cos(2m\varphi)) \\
&\quad + \frac{1}{4}(1-\cos(2l\varphi))(1-\cos(2m\varphi)) + \\
&\quad - \frac{1}{2}\left[\cos((l-m)\varphi) + \cos((l+m)\varphi)\right] \\
&\quad \left[\cos((l-m)\varphi) - \cos((l+m)\varphi)\right]\mathrm{d}\varphi \\
&= \int_0^{2\pi} \Big[\frac{1}{2} - \frac{1}{4}\big(\cos(2(l-m)\varphi) \\
&\quad - \cos(2(l+m)\varphi)\big)\Big]\,\mathrm{d}\varphi \\
&= \pi
\end{aligned}$$

which proves Eq. (50) for the considered two pairs of mode. For all the other choices of a pair $(\boldsymbol{p}_a, \boldsymbol{p}_b)$ (i.e., for any other pair of vector modes), the same result can be proven with similar steps as the ones above.

Appendix E
Closed-Form Expressions for the Nonlinear Coefficients for Step-Index Fibers

The derivation of closed-form expressions for the nonlinear coupling coefficients in SIMMFs has few differences compared to GIMMFs. Firstly, the dependence of γ on R and on Δ is not the same as for GIMMFs. This is because for a SIMMF, instead of Eq. (22), the fitted relation for the spot-size of the Gaussian approximation is [59, Eq.8]

$$\frac{r_0}{R} = A + \frac{B}{V^{1.5}} + \frac{C}{V^6} \quad (55)$$

where $A = 0.65$, $B = 1.619$, $C = 2.879$, and we have verified the last term to be negligible in our case.

The variational approach formula for a SIMMF yields [40, Table 15-2]

$$\frac{r_0}{R} \propto \frac{1}{\sqrt{\log V}} \quad (56)$$

which, however, we have verified to be less accurate than Eq. (55). Hence, when R is varied fixed Δ, with the help of Eqs. (21), (55) and (11) it is found that

$$\mathcal{A}_{11} \approx \pi \left(\frac{A}{\mathrm{NA}k_0}\right)^2 2M \left(A + \frac{B}{(2M)^{0.75}}\right)^2 \quad (57)$$

If Δ is varied, while keeping R fixed, then

$$\mathcal{A}_{11} \approx \pi R^2 \left(A + \frac{B}{(2M)^{0.75}}\right)^2 \quad (58)$$

As a side note, $\mathcal{A}_{11}$ increases slower than in a GIMMF when R is fixed, and decreases slower when Δ is fixed, due to the different relations between r_0 and V.

We observed the numerical results to agree well with the theoretical scaling laws $M\cdot\left(A+\frac{B}{(2M)^{0.75}}\right)^2$ and $\left(A+\frac{B}{(2M)^{0.75}}\right)^2$, see Fig.10, but for slightly different proportionality factors than $\pi\left(\frac{A}{\mathrm{NA}k_0}\right)^2\cdot 2$ and πR^2.

The decrease of κ with M is numerically found to be essentially constant (thus weaker than $1/\sqrt{M}$ for GIMMFs), see Fig.11, even though we did not provide an analytic derivation of κ as for GIMMFs. Ideally, it would be possible to consider the weakly guiding analytic expressions for the modal profiles of SIMMFs, which depend on Bessel functions [40, Table 14-6], and follow a procedure analogous to the one for GIMMFs in Appendix C. For this purpose, formulas for integrals involving squares of Bessels functions (and their products) given in [60, p.431] and in [61, Eq.14] could be useful.

Appendix F
Nonlinearity Coefficient for Non-Parabolic Graded Index Fibers

The deviations in $\gamma\kappa$ in case of non-parabolic GIMMF could be ideally studied with a similar approach to the one in Section IV. That is, by independently approximating γ (or, equivalently, $\mathcal{A}_{11}$) and κ. Strictly speaking, it would be necessary to recompute also the cutoff frequencies and, hence, a substitute relation for Eq. (10). However, given the grading exponent $g=2+\delta$, with $\delta\in[-10\,\%,+10\%]$ (conservative realistic range [31]), it can be safely assumed that Eq. (10) is almost untouched.

Concerning κ, an analytic derivation in the sense of Appendix C would be quite involved because of the non-trivial expressions of the modal profiles. Extensive computations with the exact numerical method could be carried out to fit a relation similar to Eq. (17) which relates κ_{ab} to M. However, we do not expect significant changes in view of a little δ, as confirmed by Fig. 12, where it is clear that the values of κ for fibers in the literature (which in general do not have a parabolic graded index) are close to the ones of parabolic GIMMFs.

For $\mathcal{A}_{11}$, it is possible to exploit the Gaussian approximation for a generic GI profile [54, Eq.11]. Then, with the same procedure as in Appendices A and B, for a generic power-law GI profile with grading exponent $g=2+\delta$, neglecting the last two terms of the Gaussian approximation for r_0/R [54, Eq.11], it holds

$$\gamma\,\kappa(\delta)\;\approx\;\frac{n_2\omega_0}{c}\,\frac{7}{2\pi R^2}\,\frac{V^{\frac{-\delta}{4+\delta}}}{\bar{A}^2} \tag{59}$$

where $\bar{A}=(\frac{2}{5}(1+4(\frac{2}{2+\delta})^{5/6}))^{0.5}$.

Then, the ratio between $\gamma\,\kappa$ of Eq. (59) and the parabolic case of Eq. (16) is given by

$$\varepsilon=\frac{\gamma\kappa\,(\delta)}{\gamma\kappa\,(\delta=0)}=V^{\frac{-\delta}{4+\delta}}\,\frac{2}{\bar{A}^2} \tag{60}$$

For $V\in[1,100]$, which covers the whole range of Fig.12, and $\delta\in[-10\,\%,+10\%]$, it has been numerically observed that the maximum excursion of ε is $\pm10\%$.

Acknowledgments

The authors acknowledge fruitful discussion with P. Serena.

References

[1] P. Sillard, K. Benyahya, D. Soma, G. Labroille, P. Jian, K. Igarashi, R. Ryf, N. K. Fontaine, G. Rademacher, and K. Shibahara, "Few-mode fiber technology, deployments, and systems," *Proceedings of the IEEE*, vol. 110, no. 11, pp. 1804–1820, 2022.

[2] T. Matsui, P. L. Pondillo, and K. Nakajima, "Weakly coupled multicore fiber technology, deployment, and systems," *Proceedings of the IEEE*, vol. 110, no. 11, pp. 1772–1785, 2022.

[3] T. Hayashi, T. Sakamoto, Y. Yamada, R. Ryf, R.-J. Essiambre, N. Fontaine, M. Mazur, H. Chen, and T. Hasegawa, "Randomly-coupled multi-core fiber technology," *Proceedings of the IEEE*, vol. 110, no. 11, pp. 1786–1803, 2022.

[4] D. Askarov and J. M. Kahn, "Long-period fiber gratings for mode coupling in mode-division-multiplexing systems," *Journal of Lightwave Technology*, vol. 33, no. 19, pp. 4032–4038, 2015.

[5] S. Ö. Arık, K.-P. Ho, and J. M. Kahn, "Group delay management and multiinput multioutput signal processing in mode-division multiplexing systems," *Journal of Lightwave Technology*, vol. 34, no. 11, pp. 2867–2880, 2016.

[6] H. Liu, H. Wen, B. Huang, R. A. Correa, P. Sillard, H. Chen, Z. Li, and G. Li, "Reducing group delay spread using uniform long-period gratings," *Scientific reports*, vol. 8, no. 1, p. 3882, 2018.

[7] K.-P. Ho and J. M. Kahn, "Chapter 11 - mode coupling and its impact on spatially multiplexed systems," in *Optical Fiber Telecommunications (Sixth Edition)*, sixth edition ed., ser. Optics and Photonics, I. P. Kaminow, T. Li, and A. E. Willner, Eds. Boston: Academic Press, 2013, pp. 491–568. [Online]. Available: https://www.sciencedirect.com/science/article/pii/B9780123969606000110

[8] C. Antonelli, A. Mecozzi, and M. Shtaif, "The delay spread in fibers for sdm transmission: dependence on fiber parameters and perturbations," *Opt. Express*, vol. 23, no. 3, pp. 2196–2202, Feb 2015. [Online]. Available: https://opg.optica.org/oe/abstract.cfm?URI=oe-23-3-2196

[9] S. Ö. Arık, K.-P. Ho, and J. M. Kahn, "Delay spread reduction in mode-division multiplexing: Mode coupling versus delay compensation," *Journal of Lightwave Technology*, vol. 33, no. 21, pp. 4504–4512, 2015.

[10] B. J. Puttnam, G. Rademacher, and R. S. Luís, "Space-division multiplexing for optical fiber communications," *Optica*, vol. 8, no. 9, pp. 1186–1203, Sep 2021. [Online]. Available: https://opg.optica.org/optica/abstract.cfm?URI=optica-8-9-1186

[11] B. Huang, N. K. Fontaine, H. Chen, J. Cang, R. Ryf, R.-J. Essiambre, T. Nagashima, T. Sasaki, and T. Hayashi, "Minimizing the modal delay spread in coupled-core two-core fiber," in *2016 Conference on Lasers and Electro-Optics (CLEO)*, 2016, pp. 1–2.

[12] G. Rademacher, R. S. Luis, B. J. Puttnam, R. Ryf, S. van der Heide, T. A. Eriksson, N. K. Fontaine, H. Chen, R.-J. Essiambre, Y. Awaji *et al.*, "A comparative study of few-mode fiber and coupled-core multi-core fiber transmission," *Journal of Lightwave Technology*, vol. 40, no. 6, pp. 1590–1596, 2022.

[13] F. M. Ferreira and F. A. Barbosa, "Maximizing the capacity of graded-index multimode fibers in the linear regime," *Journal of Lightwave Technology*, vol. 42, no. 5, pp. 1626–1633, 2024.

[14] P. Sillard, M. Bigot, K. de Jongh, F. Achten, G. Rademacher, R. Luís, and B. Puttnam, "55-spatial-mode fiber for space division multiplexing," in *2023 Optical Fiber Communications Conference and Exhibition (OFC)*. IEEE, 2023, pp. 1–3.

[15] L. Palmieri and A. Galtarossa, "Intramodal dispersion properties of step-index few-mode spun fibers," *Journal of Lightwave Technology*, vol. 34, no. 2, pp. 303–313, 2016.

[16] G. Di Sciullo, M. van den Hout, G. Rademacher, R. S. Luis, B. J. Puttnam, N. K. Fontaine, R. Ryf, C. Haoshuo, M. Mazur, D. T. Neilson, P. Sillard, F. Achten, J. Sakaguchi, C. Okonkwo, A. Mecozzi, C. Antonelli, and H. Furukawa, "Reduction of modal dispersion in a long-haul 15-mode fiber link by means of mode permutation," in *2023 European Conference on Optical Communications (ECOC)*, 2023, pp. 250–253(3). [Online]. Available: https://digital-library.theiet.org/content/conferences/10.1049/icp.2023.2052

[17] G. Rademacher, R. S. Luis, B. J. Puttnam, N. K. Fontaine, M. Mazur, H. Chen, H. Chen, R. Ryf, D. T. Neilson, D. Dahl, J. Carpenter, P. Sillard, F. Achten, M. Bigot, J. Sakaguchi, and H. Furukawa, "3.56 peta-bit/s c+l band transmission over a 55-mode multi-mode fiber," in *2023 European Conference on Optical*

Communications (ECOC), 2023, pp. 9–12(3). [Online]. Available: https://digital-library.theiet.org/content/conferences/10.1049/icp.2023.1834

[18] P. J. Winzer and D. T. Neilson, "From scaling disparities to integrated parallelism: A decathlon for a decade," *Journal of Lightwave Technology*, vol. 35, no. 5, pp. 1099–1115, 2017.

[19] C. Antonelli, M. Shtaif, and A. Mecozzi, "Modeling of nonlinear propagation in space-division multiplexed fiber-optic transmission," *Journal of Lightwave Technology*, vol. 34, no. 1, pp. 36–54, 2016.

[20] P. Carniello, F. M. Ferreira, and H. Norbert, "Scaling of the nonlinear coupling coefficient in multimode fibers," in *2023 European Conference on Optical Communications (ECOC)*, 2023, pp. 1394–1397(3). [Online]. Available: https://digital-library.theiet.org/content/conferences/10.1049/icp.2023.2554

[21] P. Serena, C. Lasagni, A. Bononi, C. Antonelli, and A. Mecozzi, "The ergodic gn model for space-division multiplexing with strong mode coupling," *Journal of Lightwave Technology*, 2022.

[22] C. Lasagni, P. Serena, A. Bononi, A. Mecozzi, and C. Antonelli, "Impact of mode dispersion on cross-phase modulation in few-mode fiber transmissions," in *2023 European Conference on Optical Communications (ECOC)*, 2023, pp. 1242–1245(3). [Online]. Available: https://digital-library.theiet.org/content/conferences/10.1049/icp.2023.2516

[23] F. J. Garcia-Gomez and G. Kramer, "Rate and power scaling of space-division multiplexing via nonlinear perturbation," *Journal of Lightwave Technology*, vol. 40, no. 15, pp. 5077–5082, 2022.

[24] S. Mumtaz, R.-J. Essiambre, and G. P. Agrawal, "Nonlinear propagation in multimode and multicore fibers: Generalization of the manakov equations," *Journal of Lightwave Technology*, vol. 31, no. 3, pp. 398–406, 2013.

[25] D. Gloge, "Weakly guiding fibers," *Applied optics*, vol. 10, no. 10, pp. 2252–2258, 1971.

[26] F. M. Ferreira, C. S. Costa, S. Sygletos, and A. D. Ellis, "Semi-analytical modelling of linear mode coupling in few-mode fibers," *Journal of Lightwave Technology*, vol. 35, no. 18, pp. 4011–4022, 2017.

[27] ——, "Nonlinear performance of few-mode fiber links with intermediate coupling," *Journal of Lightwave Technology*, vol. 37, no. 3, pp. 989–999, 2019.

[28] S. Buch, S. Mumtaz, R.-J. Essiambre, A. M. Tulino, and G. P. Agrawal, "Averaged nonlinear equations for multimode fibers valid in all regimes of random linear coupling," *Optical Fiber Technology*, vol. 48, pp. 123–127, 2019.

[29] G. Keiser, *Optical Fiber Communications, Fourth Edition*. McGraw-Hill, 2011.

[30] P. Sillard, M. Bigot-Astruc, and D. Molin, "Few-mode fibers for mode-division-multiplexed systems," *Journal of Lightwave Technology*, vol. 32, no. 16, pp. 2824–2829, 2014.

[31] F. M. Ferreira, D. Fonseca, and H. J. A. da Silva, "Design of few-mode fibers with m-modes and low differential mode delay," *Journal of Lightwave Technology*, vol. 32, no. 3, pp. 353–360, 2014.

[32] P. Sillard, D. Molin, M. Bigot-Astruc, K. De Jongh, F. Achten, J. E. Antonio-López, and R. Amezcua-Correa, "Micro-bend-resistant low-differential-mode-group-delay few-mode fibers," *Journal of Lightwave Technology*, vol. 35, no. 4, pp. 734–740, 2017.

[33] W. Hermann and D. U. Wiechert, "Refractive index of doped and undoped pcvd bulk silica," *Materials research bulletin*, vol. 24, no. 9, pp. 1083–1097, 1989.

[34] S. Ö. Arık, D. Askarov, and J. M. Kahn, "Adaptive frequency-domain equalization in mode-division multiplexing systems," *Journal of Lightwave Technology*, vol. 32, no. 10, pp. 1841–1852, 2014.

[35] K. T. Kernetzky, "Numerical optimization of ultra-broadband wavelength conversion in nonlinear optical waveguides," Ph.D. dissertation, Technische Universität München, 2022.

[36] K. Kawano and T. Kitoh, *Introduction to Optical Waveguide Analysis: Solving Maxwell's Equation and the Schrödinger Equation*. John Wiley & Sons, 2004.

[37] F. Schmidt and K. Petermann, "Investigation of lp- and vector-modes for the analysis of space-division multiplexed systems in the nonlinear regime," *Journal of Lightwave Technology*, vol. 35, no. 22, pp. 4859–4864, 2017.

[38] C. Antonelli, A. Mecozzi, M. Shtaif, and P. J. Winzer, "Nonlinear propagation equations in fibers with multiple modes—transitions between representation bases," *Apl Photonics*, vol. 4, no. 2, p. 022806, 2019.

[39] T. I. Lukowski and F. P. Kapron, "Parabolic fiber cutoffs: A comparison of theories," *J. Opt. Soc. Am.*, vol. 67, no. 9, pp. 1185–1187, Sep 1977. [Online]. Available: https://opg.optica.org/abstract.cfm?URI=josa-67-9-1185

[40] A. W. Snyder and J. D. Love, *Optical Waveguide Theory*. Chapman and Hall, 1983.

[41] "Corning smf-28e+ optical fiber," Corning Incorporated, November 2021. [Online]. Available: https://www.corning.com/media/worldwide/coc/documents/Fiber/product-information-sheets/PI1463_07-14_English.pdf

[42] R. Ryf and C. Antonelli, "Space-division multiplexing," *Springer Handbook of Optical Networks*, pp. 353–393, 2020.

[43] P. Carniello and F. M. Ferreira, "Nonlinearity coefficients of multimode fibers," 2024. [Online]. Available: https://mediatum.ub.tum.de/1736915

[44] M.-J. Li, B. Hoover, S. Li, S. Bickham, S. Ten, E. Ip, Y.-K. Huang, E. Mateo, Y. Shao, and T. Wang, "Low delay and large effective area few-mode fibers for mode-division multiplexing," in *2012 17th Opto-Electronics and Communications Conference*. IEEE, 2012, pp. 495–496.

[45] K. Sato, R. Maruyama, N. Kuwaki, S. Matsuo, and M. Ohashi, "Optimized graded index two-mode optical fiber with low dmd, large a eff and low bending loss," *Optics express*, vol. 21, no. 14, pp. 16 231–16 238, 2013.

[46] R. Ryf, N. K. Fontaine, H. Chen, B. Guan, S. Randel, N. Sauer, S. B. Yoo, A. Koonen, R. Delbue, P. Pupalaikis *et al.*, "23 tbit/s transmission over 17-km conventional 50-μm graded-index multimode fiber," in *Optical Fiber Communication Conference*. Optica Publishing Group, 2014, pp. Th5B–1.

[47] T. Mori, T. Sakamoto, M. Wada, T. Yamamoto, and F. Yamamoto, "Few-mode fibers supporting more than two lp modes for mode-division-multiplexed transmission with mimo dsp," *Journal of Lightwave Technology*, vol. 32, no. 14, pp. 2468–2479, 2014.

[48] P. Sillard, D. Molin, M. Bigot-Astruc, K. De Jongh, F. Achten, A. M. Velázquez-Benítez, R. Amezcua-Correa, and C. M. Okonkwo, "Low-differential-mode-group-delay 9-lp-mode fiber," *Journal of Lightwave Technology*, vol. 34, no. 2, pp. 425–430, 2016.

[49] P. Sillard, D. Molin, M. Bigot-Astruc, A. Amezcua-Correa, K. de Jongh, and F. Achten, "50 um multimode fibers for mode division multiplexing," *Journal of Lightwave Technology*, vol. 34, no. 8, pp. 1672–1677, 2016.

[50] P. Sillard, D. Molin, M. Bigot-Astruc, K. de Jongh, and F. Achten, "Rescaled multimode fibers for mode-division multiplexing," *Journal of Lightwave Technology*, vol. 35, no. 8, pp. 1444–1449, 2017.

[51] A. B. Fallahkhair, K. S. Li, and T. E. Murphy, "Vector finite difference modesolver for anisotropic dielectric waveguides," *Journal of Lightwave Technology*, vol. 26, no. 11, pp. 1423–1431, 2008.

[52] M. Hashimoto, "Cutoff frequencies of vector wave modes in cladded inhomogeneous optical fibre," *Electronics Letters*, vol. 21, no. 16, pp. 806–808, 1980.

[53] G. P. Agrawal, *Fiber-Optic Communication Systems*. John Wiley & Sons, 2021.

[54] D. Marcuse, "Gaussian approximation of the fundamental modes of graded-index fibers," *J. Opt. Soc. Am.*, vol. 68, no. 1, pp. 103–109, Jan 1978. [Online]. Available: https://opg.optica.org/abstract.cfm?URI=josa-68-1-103

[55] A. Mafi, "Pulse propagation in a short nonlinear graded-index multimode optical fiber," *Journal of Lightwave Technology*, vol. 30, no. 17, pp. 2803–2811, 2012.

[56] G. B. Arfken, H. J. Weber, and F. E. Harris, *Mathematical methods for physicists: a comprehensive guide*. Academic press, 2011.

[57] Y. Jiang, G. Ren, W. Jin, Y. Xu, W. Jian, and S. Jian, "Polarization properties of fiber-based orbital angular momentum modes," *Optical Fiber Technology*, vol. 38, pp. 113–118, 2017.

[58] J. Miller, "Formulas for integrals of products of associated legendre or laguerre functions," *Mathematics of Computation*, vol. 17, no. 81, pp. 84–87, 1963.

[59] D. Marcuse, "Loss analysis of single-mode fiber splices," *The Bell System Technical Journal*, vol. 56, no. 5, pp. 703–718, 1977.

[60] W. Rosenheinrich, "Tables of some indefinite integrals of bessel functions," *University of Applied Sciences, Germany*, 2022. [Online]. Available: https://www.eah-jena.de/fileadmin/user_upload/eah-jena.de/fachbereich/gw/Ehemalige/rosenheinrich/besint.pdf

[61] E. Matagne, "Some integrals involving squares of bessel functions and generalized legendre polynomials," *Advanced Electromagnetics*, vol. 11, no. 4, pp. 80–83, 2022.